A fully coupled method for numerical modeling and dynamic analysis of floating vertical axis wind turbines

Zhengshun Cheng[a,b,c,*], Helge Aagaard Madsen[d], Zhen Gao[a,b,c], Torgeir Moan[a,b,c]

[a] *Department of Marine Technology, Norwegian University of Science and Technology (NTNU), Trondheim, NO-7491, Norway*
[b] *Centre for Ships and Ocean Structures (CeSOS), NTNU, Trondheim, NO-7491, Norway*
[c] *Centre for Autonomous Marine Operations and Systems (AMOS), NTNU, Trondheim, NO-7491, Norway*
[d] *Department of Wind Energy, Technical University of Denmark, Roskilde, 4000, Denmark*

Abstract

Offshore wind energy is one of the most promising renewable energy resources and an increasing interest arises to develop floating vertical axis wind turbines (VAWTs), which have the potential to reduce the cost of energy. Assessment of the performance of floating VAWTs requires sophisticated fully coupled aero-hydro-servo-elastic simulation tools, which are currently limited. This paper aims to develop a fully integrated simulation tool for floating VAWTs. Based on the actuator cylinder (AC) flow model, aerodynamic modeling of floating VAWTs is established with consideration of the effects of turbulence, dynamic inflow and dynamic stall. The developed aerodynamic code is then coupled with the code SIMO-RIFLEX to achieve a fully coupled tool, i.e. SIMO-RIFLEX-AC, which can account for the aerodynamic, hydrodynamics, structural dynamics and controller dynamics with high fidelity. A series of code-to-code comparisons with the codes HAWC2 and SIMO-RIFLEX-DMS are carried out using a land-based VAWT and a semi VAWT, and reveal that the present code can predict the aerodynamic loads and dynamic responses accurately. Moreover, the code SIMO-RIFLEX-AC can predict more accurate responses than the code SIMO-

---

[*] Corresponding author

Email address: `zhengshun.cheng@ntnu.no, zhengshun.cheng@gmail.com` (Zhengshun Cheng)

RIFLEX-DMS, such as the platform motions, tower base bending moments and tension in mooring lines.

Keywords: Floating vertical axis wind turbine, fully coupled method, aero-hydro-servo-elastic, actuator cylinder flow model

---

1. Introduction

During the 1970s and 1980s, a substantial amount of researches were conducted to develop the vertical axis wind turbines (VAWTs), particularly in the United States and Canada. The largest onshore VAWT, the Éole Darrieus wind turbine, was built in 1986 at Québec, Canada. Commercial development of VAWTs was made in the United States during the 1980s by FloWind Ltd. However, due to fatigue problems within the bearings and blades, VAWTs lost the ground relative to the horizontal axis wind turbines (HAWTs).

In recent years, offshore wind farms are moving towards deeper waters and the interest in the development of floating VAWTs has been resurging. Compared with floating HAWTs, floating VAWTs have lower centers of gravity, are independent of wind direction, can provide reduced machine complexity and have the potential of achieving more than 20% cost of energy reductions [1]. Moreover, floating platform can help to mitigate the fatigue damage suffered by the onshore VAWTs [2]. In addition, floating VAWTs are more suitable for deployment as wind farms than floating HAWTs, because they are less affected by wake effects. The wake generated by a pair of counter-rotating H-rotors dissipate more quickly than that of floating HAWTs, allowing them to be deployed with small separations [3]. Thus, more and more efforts are devoted to the development of floating VAWTs. In order to assess the technical feasibility of floating VAWTs, a fully coupled simulation tool is required. However, currently the simulation tools which are capable of performing fully coupled analysis of floating VAWTs are very limited, due to the difficulty of predicting the aerodynamic loads accurately at a small computational cost.

Since Sandia National Laboratories started the study of VAWTs in the 1970s, a variety of aerodynamic models have been used to predict aerodynamic loads acting on the rotor for VAWTs. These include multi-streamtube model, double multi-streamtube (DMS) model, actuator cylinder (AC) flow model, panel method, vortex method and computational fluid dynamics (CFD) method. A comprehensive overview of these models can refer to Borg et al. [4].

Among these models, currently the DMS model has been widely used to estimate the aerodynamic loads on VAWTs. The DMS is also adopted in several available fully coupled simulation tools, including the SIMO-RIFLEX-DMS [5], FloVAWT [6] and OWENS [7]. The SIMO-RIFLEX-DMS code was developed by Wang et al. [5] to perform the fully coupled non-linear aero-hydro-servo-elastic simulations for floating VAWTs. This code is based on the SIMO [8] and RIFLEX [9] programs which have been extensively used and validated for offshore structures subjected to wave loads. It can account for the turbulent wind inflow, aerodynamics, hydrodynamics, control dynamics, structural mechanics and mooring line dynamics. The aerodynamic loads are calculated using the DMS model with the Beddoes-Leishman dynamic stall model. To provide a simplified coupled dynamics design tool to the use in the preliminary design stages of floating VAWTs, Collu et al. [6] from Cranfield University developed FloVAWT (Floating Vertical Axis Wind Turbines) code. The DMS model with Gormont-Berg dynamic stall is used in the aerodynamic model. However, this code is based on a simplified quasi-static mooring line model and structural and controller dynamics are not accounted for. Sandia National Laboratories developed the OWENS (Offshore Wind ENergy Simulation) toolkit [7] aiming at establishing a robust and flexible finite element framework and VAWT mesh generation utility, coupled with a modular interface that allows users to integrate easily with existing codes, such as aerodynamic and hydrodynamic codes.

However, by considering a 2D VAWT rotor, Ferreira et al. [10] compares the different models used to model the VAWT, including the multi-streamtube model, the DMS model, the AC model, a 2D potential flow panel model, a 3D unsteady lifting line model and a 2D conformal mapping unsteady vortex model. The comparison reveals that the DMS model proves to be fundamentally incorrect in the prediction of the effect of changing the fixed pitch angle, and that the AC model shows a good agreement with the panel and vortex models. Moreover, Roscher [11] compares these models with respect to complexity, accuracy, computational cost, suitability for optimization and aeroelastic analysis. Due to the consideration of accuracy and computational cost, the AC model is the favorable method that can be used for aero-hydro-servo-elastic time domain simulations for floating VAWTs.

The AC model is originally developed by Madsen [12] in his PhD study. The AC model has been implemented in HAWC2 [13, 14] to conduct the fully coupled aero-hydro-servo-elastic time domain simulations for floating VAWTs. It can account for dynamic inflow, structural dynamics, tower shadow and dynamic stall. Paulsen et al. [15] performed a design optimization of the proposed DeepWind concept. An improved design has been obtained with an optimized blade profile with less weight and higher stiffness than the 1st baseline design.

In the present study an aerodynamic code is developed using the AC model. Induction calculation using the AC method is firstly described. Latter aerodynamic modeling of floating VAWTs is established with consideration of the effects of dynamic stall, turbulent and dynamic inflow. Then this aerodynamic code is coupled with SIMO-RIFLEX to achieve a fully coupled aero-hydro-servo-elastic simulation tool with high fidelity. Using a landbased VAWT and a semi VAWT, a series of numerical simulations are carried out to verify the fully coupled tool. This paper presents the development and the validation of the fully coupled simulation tool, SIMO-RILFEX-AC. It can account for the turbulent inflow, aerodynamics, hydrodynamics, structural dynamics, controller dynamics and mooring line dynamics. This tool can be used in the integrated dynamic analysis of floating VAWTs to reveal and demonstrate the characteristics of different floating VAWT systems.

2. Aerodynamic Modeling of floating VAWTs

Each blade of a VAWT can be divided into a number of elements. When the VAWT rotates, each element creates a cylinder tube that is perpendicular to the shaft. The swept surface created by the VAWT can then be divided approximately into a number of vertically stacked cylinders with finite height and with a radius coinciding with the rotor radius at the actual position along the shaft. Therefore the complex 3D flow problem is condensed into a number of 2D actuator cylinder flow problems. For each cylinder, the AC method, developed by Madsen [12], is used to find out the induced velocity.

In this section, the aerodynamic modeling of floating VAWTs using the AC method is presented, as the flow chart illustrated in Figure 1. The effects of wind shear, turbulence, dynamic stall and dynamic inflow are also taken into account in the present implementation.

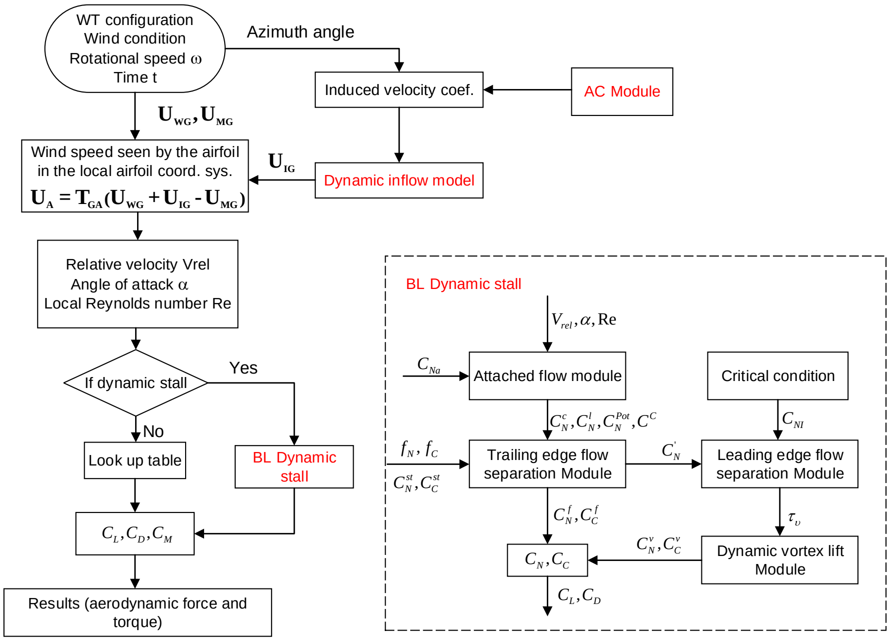

Figure 1: Flow chart of modeling of a floating VAWT using AC method. The models of dynamic inflow and dynamic stall are included.

2.1. Aerodynamic loads on a 2D VAWT

For each calculation point in the local airfoil coordinate system , the local inflow velocity $\mathbf{V_A}$ seen at a blade section can be determined from

$$\mathbf{V_A} = \mathbf{T_{GA}} \left(\mathbf{V_{WG}} + \mathbf{V_{IG}} - \mathbf{V_{MG}} \right) \tag{1}$$

where $\mathbf{T_{GA}}$ is a transformation matrix from global to airfoil-fixed coordinate system. The global inflow velocity $\mathbf{V_G}$ seen at a blade section is the vector sum of the free wind speed $\mathbf{V_{WG}}$, the induced velocity $\mathbf{V_{IG}}$ and subtracting the velocity due to the motion $\mathbf{V_{MG}}$. $\mathbf{V_{MG}}$ is comprised of the blade rotation, the translational and rotational velocity from the platform and the velocity due to the elastic deformation of the blades. The induced velocity $\mathbf{V_{IG}}$ can be calculated using the AC method by assuming a 2D quasi-static flow problem, which is described latter.

Therefore, a 2D look-up table giving the relationship between the coefficients C_l, C_d and the angle of attack α is used to compute the aerodynamic lift and drag force, as well as the tangential load F_{tA} and normal load F_{nA} acting on the local element. In the AC method, the tangential and normal loads are non-dimensionalized as follows [16]

$$Q_t = -\frac{BF_{tA}}{2\pi R \rho V_{wB}^2 \sin(\beta)} \tag{2}$$

$$Q_n = \frac{BF_{nA}}{2\pi R \rho V_{wB}^2 \sin(\beta)} \tag{3}$$

where B is the number of blades, ρ the air density, R the radius of the disk considered, β the blade angle with the vertical direction, and V_{wB} the local free wind speed.

2.2. Actuator Cylinder Flow Model

The AC method is a quasi-steady Eulerian model. The model extends the actuator disc concept to an actuator surface coinciding with the swept area of the 2D VAWT. In the AC model, the normal and tangential forces Q_n and Q_t

resulting from the blade forces are applied on the flow as volume force perpendicular and tangential to the rotor plane, respectively, as illustrated in Figure 2. Thus the induced velocities w_x and w_y are related to volume forces as well as the normal and tangential loads Q_n and Q_t based on the Euler equation and continuity equation. In this way, the final velocity can be divided into a linear part which is a function of the prescribed normal and tangential loads Q_n and Q_t and a nonlinear part that is a function of the induced forces. Detailed derivations regarding this 2D quasi-static flow problem can refer to Madsen et al. [13].

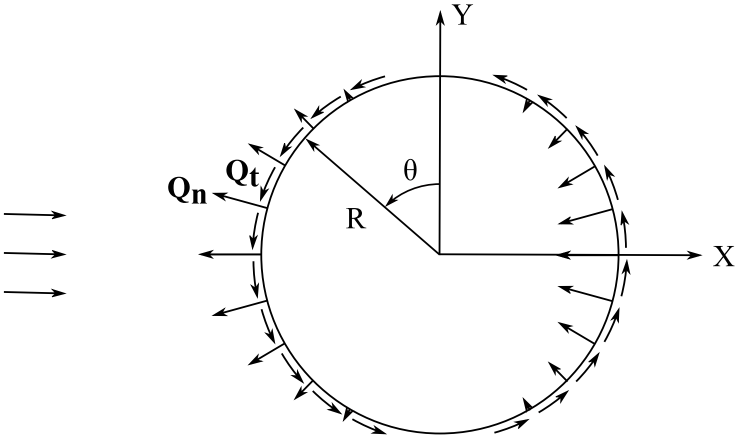

Figure 2: The actuator cylinder flow model representation of a VAWT with volume forces normal and tangential to the circle. Note that the force direction is from the VAWT noto the flow [13].

2.2.1. Linear solution

The linear solution of the induced velocities can be analytically computed, which is given by Cheng et al. [16] as follows.

$$
\begin{aligned}
w_x = & -\frac{1}{2\pi}\int_0^{2\pi} Q_n(\theta)\frac{-(x+\sin\theta)\sin\theta+(y-\cos\theta)\cos\theta}{(x+\sin\theta)^2+(y-\cos\theta)^2}d\theta \\
& -\frac{1}{2\pi}\int_0^{2\pi} Q_t(\theta)\frac{-(x+\sin\theta)\cos\theta-(y-\cos\theta)\sin\theta}{(x+\sin\theta)^2+(y-\cos\theta)^2}d\theta \\
& -\left(Q_n(\arccos y)\right)^{*}+\left(Q_n(-\arccos y)\right)^{**} \\
& -\left(Q_t(\arccos y)\frac{y}{\sqrt{1-y^2}}\right)^{*}-\left(Q_t(-\arccos y)\frac{y}{\sqrt{1-y^2}}\right)^{**}
\end{aligned}
\tag{4}
$$

$$
\begin{aligned}
w_y = & -\frac{1}{2\pi}\int_0^{2\pi} Q_n(\theta)\frac{-(x+\sin\theta)\cos\theta-(y-\cos\theta)\sin\theta}{(x+\sin\theta)^2+(y-\cos\theta)^2}d\theta \\
& -\frac{1}{2\pi}\int_0^{2\pi} Q_t(\theta)\frac{(x+\sin\theta)\sin\theta-(y-\cos\theta)\cos\theta}{(x+\sin\theta)^2+(y-\cos\theta)^2}d\theta
\end{aligned}
\tag{5}
$$

where θ is the azimuth angle, the term marked with $*$ in Eq. 4 shall only be added inside the cylinder whereas in the wake behind the cylinder both the term marked with $*$ and $**$ shall be added. Compared with the results in [13], the effect of tangential load on the computed induced velocity is considered here.

Assuming that the loading is piecewise constant, the integral part in Eqs. 4 and 5 can be rewritten as

$$
\begin{aligned}
w_x = & -\frac{1}{2\pi}\sum_{i=1}^{i=N} Q_{n,i}\int_{\theta_i-\frac{1}{2}\Delta\theta}^{\theta_i+\frac{1}{2}\Delta\theta} \frac{-(x+\sin\theta)\sin\theta+(y-\cos\theta)\cos\theta}{(x+\sin\theta)^2+(y-\cos\theta)^2}d\theta \\
& -\frac{1}{2\pi}\sum_{i=1}^{i=N} Q_{t,i}\int_{\theta_i-\frac{1}{2}\Delta\theta}^{\theta_i+\frac{1}{2}\Delta\theta} \frac{-(x+\sin\theta)\cos\theta-(y-\cos\theta)\sin\theta}{(x+\sin\theta)^2+(y-\cos\theta)^2}d\theta
\end{aligned}
\tag{6}
$$

$$
\begin{aligned}
w_y = & -\frac{1}{2\pi}\sum_{i=1}^{i=N} Q_{n,i}\int_{\theta_i-\frac{1}{2}\Delta\theta}^{\theta_i+\frac{1}{2}\Delta\theta} \frac{-(x+\sin\theta)\cos\theta-(y-\cos\theta)\sin\theta}{(x+\sin\theta)^2+(y-\cos\theta)^2}d\theta \\
& +\frac{1}{2\pi}\sum_{i=1}^{i=N} Q_{t,i}\int_{\theta_i-\frac{1}{2}\Delta\theta}^{\theta_i+\frac{1}{2}\Delta\theta} \frac{-(x+\sin\theta)\sin\theta+(y-\cos\theta)\cos\theta}{(x+\sin\theta)^2+(y-\cos\theta)^2}d\theta
\end{aligned}
\tag{7}
$$

where N is the total number of calculation points, $\Delta\theta = \frac{2\pi}{N}$ and $\theta_i = \frac{\pi}{N}(2i-1)$ for $i = 1, 2, ..., N$.

Since only induced velocities at the cylinder are of concern, the total velocity solution at the calculation point (x_j, y_j) (for $j = 1, 2, ..., N$) on the cylinder can then be rewritten as

$$w_{x,j} = -\frac{1}{2\pi}\left(\sum_{i=1}^{i=N} Q_{n,i} I_{1,i,j} + \sum_{i=1}^{i=N} Q_{t,i} I_{2,i,j}\right) - \left(Q_{n,N+1-j}\right)^* - \left(Q_{t,N+1-j}\frac{y_j}{\sqrt{1-y_j^2}}\right)^* \tag{8}$$

$$w_{y,j} = -\frac{1}{2\pi}\left(\sum_{i=1}^{i=N} Q_{n,i} I_{2,i,j} - \sum_{i=1}^{i=N} Q_{t,i} I_{1,i,j}\right) \tag{9}$$

where the terms marked with $*$ in Eqs. 8 and 9 are only added for $j > \frac{N}{2}$ (the leeward part of the AC with $x_j > 0$). $I_{1,i,j}$ and $I_{2,i,j}$ are influence coefficients at point j influenced by other point i and are given by

$$I_{1,i,j} = \int_{\theta_i - \frac{1}{2}\Delta\theta}^{\theta_i + \frac{1}{2}\Delta\theta} \frac{-\left(x_j + \sin\theta\right)\sin\theta + \left(y_j - \cos\theta\right)\cos\theta}{\left(x_j + \sin\theta\right)^2 + \left(y_j - \cos\theta\right)^2} d\theta \tag{10}$$

$$I_{2,i,j} = \int_{\theta_i - \frac{1}{2}\Delta\theta}^{\theta_i + \frac{1}{2}\Delta\theta} \frac{-\left(x_j + \sin\theta\right)\cos\theta - \left(y_j - \cos\theta\right)\sin\theta}{\left(x_j + \sin\theta\right)^2 + \left(y_j - \cos\theta\right)^2} d\theta \tag{11}$$

in which $x_j = -\sin(j\Delta\theta - \frac{1}{2}\Delta\theta)$, $y_j = \cos(j\Delta\theta - \frac{1}{2}\Delta\theta)$. It can be found that the influence coefficients $I_{1,i,j}$ and $I_{2,i,j}$ are irrespective of time and can thus be integrated once and for all.

2.2.2. Modified linear solution

It's to some extent time-consuming to compute the nonlinear solution directly. In order to make the final solution in better agreement with the fully nonlinear solution, a correction is required for the linear solution. A simple correction [13] is suggested by multiplying the velocities from the linear solution w_x and w_y with a factor k_a that is related to the axial induction factor. However, Cheng et al. [16] stated that the correction proposed by Madsen et al.[13] can give some deviation in the power coefficient at high tip speed ratios when comparing with experiments. Thus a new modification which corrects the

k_a at a high induction factor, which corresponds to a large tip speed ratio, is proposed by Cheng et al. [16].

$$k_a = \begin{cases} \frac{1}{1-a}, & (a \leq 0.15) \\ \frac{1}{1-a}(1 - 0.35\,(1 - \exp\,(-4.5(a - 0.15)))), & (a > 0.15) \end{cases} \tag{12}$$

where the induction factor a is found based on a relationship between the induction a and the average thrust coefficient C_T.

2.3. Wind inflow

The effects of wind shear and turbulence can be included in the local free wind speed. The wind inflow can be determined using the hub height wind file, full field wind file and user-defined wind file. For the turbulent wind inflow, the three dimensional turbulent wind fields are generated using the NREL's TurbSim program [17].

2.4. Dynamic stall model

In this work, the Beddoes-Leishman dynamic stall model is used to predict the VAWT's aerodynamic loads. It is a semi-empirical model which can represent the physical phenomenon to a certain extent through a superposition of separate indicial functions. The Beddoes-Leishman model is original developed to simulate the dynamic stall effect on the helicopter [18]. The adaptation of this model has been studied for HAWTs by Gupta and Leishman [19] and VAWTs by Dyachuk et al. [20].

The Beddoes-Leishman model consists of three parts: unsteady attached flow, unsteady separated flow and dynamic vortex lift. In the unsteady attached flow regime, the aerodynamic loads are comprised of a circulatory component related to the change of the angle of attack and an impulsive component related to the change rate of the angle of attack and pitch moment. Thus the total normal force coefficient C_N under the attached flow condition can be written as

$$C_N = C_N^C + C_N^I \tag{13}$$

where C_N^C and C_N^I are the circulatory and impulsive normal force coefficients, respectively. The unsteady chordwise force coefficient C_C is based on the circulatory component of C_N.

The calculated attached flow response is then modified due to the flow separation on the low-pressure side of the airfoil. The unsteady separate flow usually includes leading edge separation and trailing edge separation. The effective separation point is related to the normal force coefficient and the chordwise force coefficient according to the Kirchhoff theory and calculated using static data. An empirically derived first order lag is then applied to the movement of the effective separation point to account for the time lag in movement of the separation point during unsteady conditions. The final main component of the model represents the vortex buildup and shedding that occurs during the dynamic stall. The vortex lift contribution is empirically modeled as an excess circulation in the vicinity of the airfoil using the difference between the attached flow C_N and the unsteady non-linear value from the Kirchhoff relationship. Therefore, the total loading on the airfoil is obtained by summing all of the aforementioned components.

Several modifications are implemented to adapt the Beddoes-Leishman model for VAWT applications, as described in the AeroDyn theory manual [21]. The model is capable of producing aerodynamic force coefficients over the entire range of possible angles of attack. To ensure proper regeneration of coefficients, two effective separation point tables are used, one for the normal force coefficient and one for the chordwise force coefficient. Moreover, the sign of the effective separation point is saved with the value of the parameter. Due to the effect of vortex component, the chordwise force coefficient is modified by adding one additional term from the vortex lift in the same manner as the circulatory component of C_N, as follows [2]

$$C_C = C_{Na}\left(\alpha_e - \alpha_0\right)\alpha_e\sqrt{f_C^{''}} + C_N^v\alpha_e\left(1-\tau_v\right) \tag{14}$$

where α_e is the effective angle of attack, α_0 is the zero-lift angle, C_{Na} is the normal force coefficient curve slope, $f_C^{''}$ is the dynamic separation point function,

C_N^v is the normal force coefficient from the vortex lift contribution and τ_v is the non-dimensional parameter to track the position of the vortex across the airfoil. Finally, the lift coefficient and drag coefficient are calculated from C_N and C_C by force resolution as

$$C_L = C_N \cos(\alpha) + C_C \sin(\alpha) \tag{15}$$

$$C_D = C_N \sin(\alpha) - C_C \cos(\alpha) + C_{d0} \tag{16}$$

where C_{d0} is the minimum drag coefficient corresponding to the zero angle of attack.

The integration of the Beddoes-Leishman dynamic stall model into the AC model in the time domain is shown in the flow chart in Figure 1. At each time step, the calculated relative velocity and the angle of attack are inputs into the Beddoes-Leishman dynamic stall model. By including the dynamic stall effect the normal force coefficient and the chordwise force coefficient are corrected and the lift coefficient and drag coefficient are thus obtained.

2.5. Dynamic inflow model

The induced velocities calculated using the AC method are based on a steady state equilibrium without time. However, the mass flow through the rotor is substantial. In order to account for the time delay before the induced velocities are in equilibrium with the aerodynamic loads, a dynamic flow model should be applied.

Currently there is none sophisticated dynamic flow models for VAWTs. The dynamic flow model proposed by Larsen and Madsen [14] is employed here. The dynamic inflow is modeled using a low pass filtering of the calculated steady state induced velocities, which is in a similar way as for a horizontal axis wind turbine. Here two first-order filters are coupled in parallel with weighted functions to model the near wake and far wake effects respectively. Assuming that the induced velocity in a previous step is denoted y_{n-1}, and the raw signal of induced velocity in the current step is denoted q, then the filtered induced velocities due to the near wake and far wake can be written as

$$y_{nw} = y_{n-1} \exp\left(-\frac{\Delta T}{\tau_{nw}}\right) + q\left(1 - \exp\left(-\frac{\Delta T}{\tau_{nw}}\right)\right) \tag{17}$$

$$y_{fw} = y_{n-1} \exp\left(-\frac{\Delta T}{\tau_{fw}}\right) + q\left(1 - \exp\left(-\frac{\Delta T}{\tau_{fw}}\right)\right) \tag{18}$$

where ΔT is the constant time step. τ_{nw} and τ_{fw} are time constants for the near wake filter and far wake filter, respectively. The time constant is non-dimensionalized with respect to the rotor radius and the average wake velocity $\tau = \tau^* \frac{R}{V_{wake}}$, in which the non-dimensional time constant τ^* is set to be approximately 0.5 and 2 for the near wake filter and far wake filter, respectively. Applying a weighed factor of 0.6 for the near wake filter and 0.4 for the far wake filter, the final filtered induced velocity is given as

$$y_n = 0.6y_{nw} + 0.4y_{fw} \tag{19}$$

3. Development of a fully coupled simulation tool

The developed AC model is then coupled with SIMO-RIFLEX to achieve a fully coupled simulation tool for evaluating the performance of floating VAWT systems. The codes SIMO and RIFLEX were developed by MARINTEK and widely used in the offshore oil and gas industry. The SIMO-RIFLEX wind turbine module has previously been verified [22, 23]. The code SIMO-RIFLEX-AC can account for the turbulent wind inflow, aerodynamics, hydrodynamics, structural dynamics and control dynamics. This coupled code, as illustrated in Figure 3, integrates three computer codes. SIMO computes the rigid body hydrodynamic forces and moments on the hull [8] ; RIFLEX serves as a nonlinear finite element solver and provides the links to an external controller and the code AC [9]; AC calculates the aerodynamic loads on the blades. The external controller, which is written in Java, is used to regulate the rotor rotational speed for VAWTs with fixed blade pitch. This combination provides a comprehensive

aero-hydro-servo-elastic simulation tool with well-known aerodynamics, sophis-
205 ticated hydrodynamics, a stable nonlinear finite element solver, and user-defined control logic.

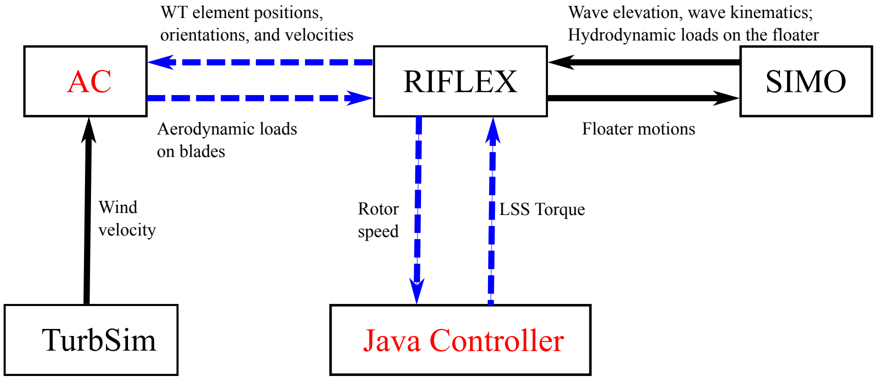

Figure 3: Overview of the fully coupled simulation tool SIMO-RIFLEX-AC (Modified based on [24].

A floating VAWT system is usually comprised of a rotor harvesting wind energy, a floater supporting the rotor and a mooring system keeping the floater in position. Figure 4 shows the structural model and external load model of a floating VAWT system in the coupled code SIMO-RIFLEX-AC. The blades, shaft, tower and mooring lines are modeled using the nonlinear flexible finite elements while the floating platform is considered as a rigid body. The dynamics of the floating platform is represented using the equation of motion proposed by [25]

$$(\mathbf{M}+\mathbf{A}_{\infty})\ddot{\mathbf{x}}(t)+\int_{-\infty}^{\infty}\kappa(t-\tau)\dot{\mathbf{x}}(t)\,d\tau+(\mathbf{K_m}(\mathbf{x})+\mathbf{K_h})\mathbf{x}(t)=\mathbf{F_{exc}}(\mathbf{x},\dot{\mathbf{x}},t) \tag{20}$$

where $\mathbf{M}$ is the mass matrix of the floating system, $\mathbf{A}_{\infty}$ is the added mass matrix at infinite frequencies, $\mathbf{x}$, $\dot{\mathbf{x}}$ and $\ddot{\mathbf{x}}$ are the displacement, velocity and acceleration of the platform, respectively. $\kappa(t-\tau)$ is the retardation function which represents the fluid memory effect. $\mathbf{K_h}$ is the hydrostatic restoring matrix and $\mathbf{K_m}$ is the nonlinear restoring matrix from the mooring system. $\mathbf{F_{exc}}$ is the excitation forces which includes the Froude-Krylov force $\mathbf{F^{FK}}$, diffraction force

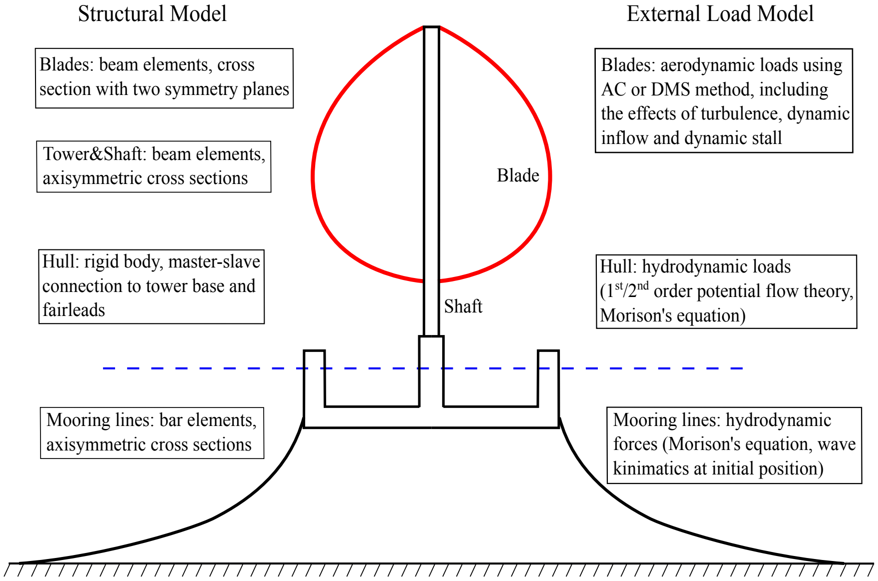

Figure 4: The structural model and external force model of a floating VAWT (Modified based on [24].)

$\mathbf{F^D}$, aerodynamic force $\mathbf{F^{Aero}}$ and hydrodynamic viscous force $\mathbf{F^{Drag}}$.

$$\mathbf{F_{exc}}\left(\mathbf{x}, \dot{\mathbf{x}}, t\right) = \mathbf{F^{FK}}\left(t\right) + \mathbf{F^{D}}\left(t\right) + \mathbf{F^{Aero}}\left(\mathbf{x}, \dot{\mathbf{x}}, t\right) + \mathbf{F^{Drag}}\left(\dot{\mathbf{x}}, t\right) \tag{21}$$

The aerodynamic force $\mathbf{F^{Aero}}$ is computed in the AC model and transfered from the rotor to the generator. While the hydrodynamic loads involved in Eqs. 20 and 21 are calculated in SIMO. At each time step, the dynamic equilibrium equations of the rotor, platform and mooring lines are solved in RIFLEX and the rotor rotational speed is regulated through the external controller. Then the platform motions are transfered to SIMO to update the hydrodynamic loads, while the positions, velocities and accelerations of the blade elements are transfered to the AC model to update the aerodynamic loads.

3.1. Aerodynamic model

The aerodynamic model, i.e. AC, has been comprehensively described above. It accounts for the effects of variation in the Reynolds number, wind shear and turbulence, dynamic stall and dynamic inflow. The induced velocity is computed based on the AC method. The Beddoes-Leishman dynamic stall model is implemented to predict the aerodynamic loads more accurately.

3.2. Hydrodynamic model

The hydrodynamic loads are computed using a combination of the potential flow theory and Morison's equation. The hydrostatic restoring coefficients are computed on the basis of the mean position of the structure. For large volume structures, the first-order potential flow theory gives the wave excitation force by solving a diffraction problem and provides the added mass and potential damping by solving a radiation problem. The added mass, radiation damping are then applied in the time domain using the convolution technique [26].

When the second-order wave force becomes important for structures with natural frequencies that either very low or near twice the wave frequency, the second-order potential flow theory is applied to account for the mean drift, difference-frequency and sum-frequency wave forces. If applicable, the Newman approximation, which is based on the solution of the first-order potential flow theory, can be adopted to represent the difference-frequency wave force. Otherwise, the quadratic transfer function (QTF) should be used for the difference-frequency and sum-frequency wave forces. Moreover, the third-order wave force can also be included if, for instance, the effect of ringing response is relevant. However, in the verification of the simulation tool in Section 4, the second-order and third-order wave forces are not considered.

Regarding the slender structures where the diameter D is small compared to the wavelength λ (roughly, $\frac{D}{\lambda} < \frac{1}{5}$), the Morison equation is applied to calculate the inertial load and viscous drag load [26]. The transverse hydrodynamic force per unit length is given by

$$dF = \rho_w \pi \frac{D^2}{4} \dot{u_w} + \rho_w \pi C_a \frac{D^2}{4} (\dot{u_w} - \dot{u_b}) + \frac{1}{2} \rho_w C_d D (u_w - u_b) \left| u_w - u_b \right| \quad (22)$$

where ρ_w is the water density, u_w is the transverse wave particle velocity, u_b is the local transverse body velocity, and C_a and C_d are the added mass and quadratic drag coefficients, respectively. In addition, viscous forces on large volume structures can also be incorporated through the Morison's equation by considering only the quadratic viscous drag term in Eq. 22. For the floating VAWT used in Section 4, the values of C_a and C_d for all members of the platform are referred to Robertson et al. [27].

3.3. Structural model

In the structural model, the blades are modeled as flexible beam elements with two symmetric planes to differ the flapwise stiffness and edgewise stiffness. The tower and shaft are modeled as axisymmetric beam elements while the mooring lines are considered as nonlinear bar element. A very short tower close to the tower base is used to connect the rotating shaft and floater through a flexible joint. The electric torque from the generator is applied at this joint to regulate the rotational speed according to the prescribed control strategy. Moreover, master-slave connections are applied to integrate the motions between the tower base and fairleads.

Therefore, the dynamic equilibrium of the whole floating VAWT system can be expressed as the following equation by assuming a linear elastic material,

$$\mathbf{M_g}\ddot{\mathbf{r}} + \mathbf{B_g}\dot{\mathbf{r}} + \mathbf{K_g}\mathbf{r} = \mathbf{R^E}\left(\mathbf{r}, \dot{\mathbf{r}}, t\right) \tag{23}$$

where $\mathbf{M_g}$, $\mathbf{B_g}$ and $\mathbf{K_g}$ are the global mass, damping and stiffness matrices, respectively. r, $\dot{r}$ and $\ddot{r}$ are the system displacement, velocity and acceleration vectors, respectively. The structural damping here is specified using the Rayleigh damping, which is a linear combination of the mass $\mathbf{M_g}$, and stiffness $\mathbf{K_g}$ matrices as in the following equation.

$$\mathbf{B_g} = \alpha_1 \mathbf{M_g} + \alpha_2 \mathbf{K_g} \tag{24}$$

In which α_1 and α_2 are the mass and stiffness proportional coefficients, respectively. In RIFLEX, the dynamic equilibrium equations can be solved in the time domain using the Newmark-β numerical integration ($\beta = 0.256$, $\gamma = 0.505$). When modeling the landbased and floating VAWTs in Section 4, the values of α_1 and α_2 are chosen as $\alpha_1 = 0$ and $\alpha_2 = 0.03$. The time step is set as $0.0025s$ for all simulations.

3.4. Control strategy

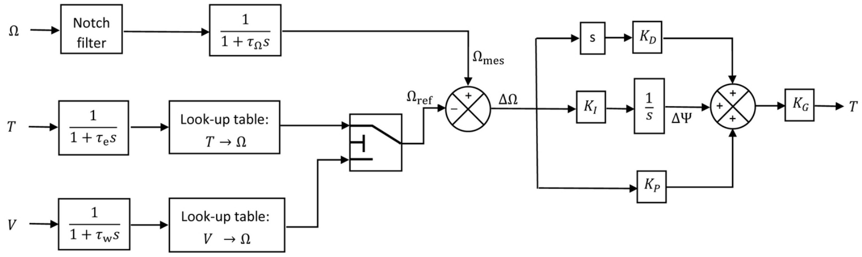

Figure 5: The generator torque control algorithm for a floating VAWT based on a PID architecture.

In the previous study, two control strategies were used to enable the variable-speed and fixed-pitch operations of a floating VAWT system [28]. The architecture of the generator torque controller is shown in Figure 5. The generator rotational speed and electric torque are measured and low-pass filtered. The controller aims to minimize the error between the measured and filtered rotational speed Ω_{mes} and the reference rotational speed Ω_{ref},

$$\Delta\Omega = \Omega_{mes} - \Omega_{ref} \tag{25}$$

in which the reference rotational speed Ω_{ref} is defined as a function of the measured wind speed $\widehat{V}$ and the measured and low-pass filtered electric torque $\widehat{T}$. The rotational speed error $\Delta\Omega$ is then fed through the proportional, integral and derivative paths to obtain an updated value of the required electric torque, as follows,

$$T(t) = K_G \left(K_P \Delta\Omega(t) + K_I \int_0^t \Delta\Omega(\tau) d\tau + K_D \frac{d}{dt} \Delta\Omega(t) \right) \tag{26}$$

in which K_G is the generator stiffness, and K_P, K_I and K_D are the proportional, integral and derivative gains, respectively.

Figure 6 presents the relationship between the reference rotational speed and the wind speed for a typical floating VAWT. According to the operating conditions, it can be divided into three regions, as highlighted in Figure 6. In region I where wind speeds ranges from V_{in} to V_{Ω_N}, the rotor operates at the optimal tip speed ratio so as to achieve the highest power coefficient. In region II, the rotor operates at a moderate tip speed ratio and holds the rotational speed constant at the rated rotational speed. The control targets in region I and II aim to maximize the power capture and at the same time keeps the rotational speed not larger than the rated one.

However, the control targets in region III shift to limit the aerodynamic loads acting on the rotor by limiting the rotational speed. In this case, the rotor rotates at relatively low tip speed ratios and two control strategies, i.e. the baseline controller and improved controller, are considered here, as illustrated in Figure 6. This baseline controller is capable of maximizing the power capture for wind speeds below V_{Ω_N} and maintaining the rotational speed for wind speeds above V_{Ω_N}, while the improved controller aims to maximize the power capture for wind speeds below V_N and maintaining the power capture approximately constant for the above rated wind speeds.

In addition, a notch filter is implemented in the controller to isolate the electric torque from the variation of aerodynamic loads. For turbulent wind conditions the wind speed is measured and low-pass filtered.

4. Verification of the fully coupled simulation tool

4.1. Wind turbine models

In this study, two wind turbine models, one landbased VAWT and one floating VAWT as depicted in Figure 7, are used to verify the code SIMO-RIFLEX-AC. The landbased VAWT considered is the 5MW Darrieus rotor developed in the DeepWind project [29]. The rotor is comprised of two blades and one rotating tower that spans from the top to the bottom which is connected to the generator. Main specifications of this rotor are summarized in Table 1. The generator considered here is assumed to be placed at the tower base.

A floating VAWT concept with a semi-submersible platform supporting the 5MW Darrieus rotor is also used to verify the code SIMO-RIFLEX-AC. This

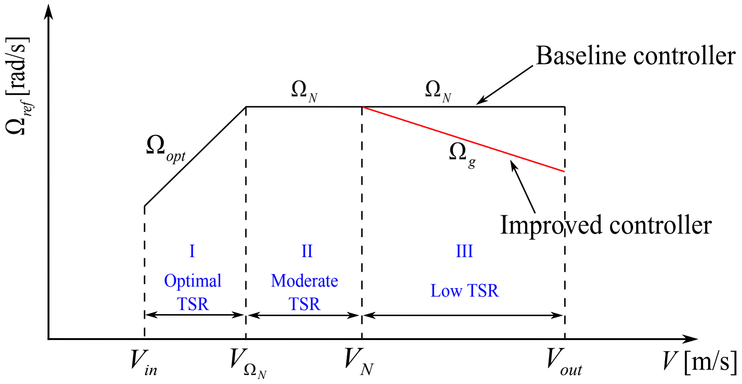

Figure 6: The relationship between the reference rotor rotational speed and the wind speed for the baseline and improved controllers. V_{in}, V_N and V_{out} are the cut-in, rated, and cut-out wind speed, respectively; V_{Ω_N} is the wind speed for the rated rotational speed; Ω_N is the rated rotational speed; Ω_{opt} is the optimal rotational speed that can maximize the power capture; Ω_g is the rotational speed that can hold the mean generator power approximately constant.

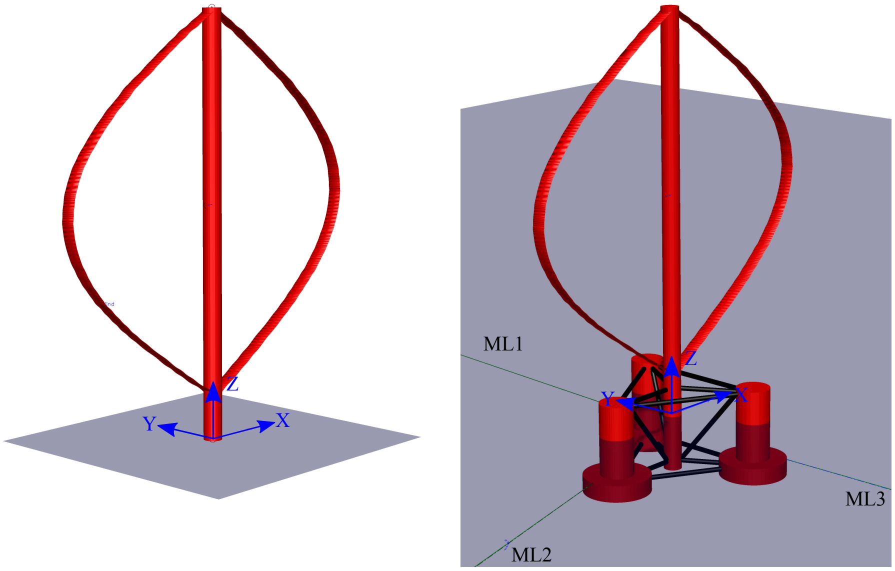

Figure 7: The landbased VAWT and semi VAWT concepts.

Table 1: Specifications of the Darrieus 5 MW wind turbine

Rated power [MW]	5
Rotor radius [m]	63.74
Rotor height, root-to-root [m]	129.56
Chord length [m]	7.45
Airfoil [-]	NACA0018
Cut-in, rated, cut-out wind speed [m/s]	5 , 14 , 25
Rated rotor rotational speed [rpm]	5.26
Total mass, including rotor, shaft and tower [kg]	754,226
Location of overall CM [m]	(0 , 0 , 75.6)

Table 2: Properties of the semi-submersible VAWT system

Water depth [m]	200
Draft [m]	20
Diameter at mean water level [m]	12.0/6.5
Platform mass, including ballast and generator [ton]	13353.7
Center of mass for platform [m]	(0, 0, -13.42)
Buoyancy in undisplaced position [kN]	139816
Center of buoyancy [m]	(0, 0, -13.15)
Surge/Sway natural period [s]	114.0
Heave natural period [s]	17.1
Roll/Pitch natural period [s]	31.0
Yaw natural period [s]	79.7

concept is proposed by Wang et al. [5] and comprehensively studied using the code SIMO-RIFLEX-DMS [30, 31, 32]. The semi-submersible platform considered was originally designed to support the NREL 5 MW wind turbine [33] in the water depth of 200 m. Here reasonable modifications are made on the platform to support the 5 MW Darrieus rotor, such as adjusting the ballast of the semi. Details regarding the adjustment can refer to Cheng et al. [30]. Properties related to the floating VAWT system are given in Table 2. The natural periods of rigid body motions for the floating system were estimated by conducting free decay tests [30].

The code SIMO-RIFLEX has been widely used and validated in the offshore oil and gas industry. Regarding the present floating wind turbine model, several verifications with respect to the structural dynamics and hydrodynamics have been carried out in the previous studies. Wang et al. [5] investigated the first 10 natural frequencies and corresponding eigen modes of the landbased VAWT using both RIFLEX and Abaqus [34]. The Lanczos's method is used in these two analyses. It is found that RIFLEX agrees quite well with Abaqus. Cheng et al. [30] studied the response amplitude operators (RAOs) of the semi VAWT subjected to wave loads using both the regular wave technique and white noise technique. The white noise technique predicts all RAOs accurately except at the resonant frequency of each mode.

In the following, verification of the code SIMO-RIFLEX-AC is to be conducted by comparison with the codes SIMO-RIFLEX-DMS and HAWC2 using the landbased VAWT and semi VAWT.

4.2. Load cases

A series of load cases were defined to verify the code SIMO-RIFLEX-AC, as given in table 3. LC1 is the steady wind condition and is used to verify the aerodynamic loads calculated using different codes. LC2 and LC3 are the steady wind and irregular wave condition, and the turbulent wind and irregular wave condition, respectively. The wind and wave are correlated and directionally aligned. They were used to verify the dynamic responses of the floating wind turbine system subjected to wind and wave loads.

Table 3: Definition of load cases

	U_W [m/s]	H_S [m]	T_P [s]	T_I [-]	Wave Cond.	Sim. Length [s]
LC1.1	8	-	-	0	-	800
LC1.2	14	-	-	0	-	800
LC1.3	18	-	-	0	-	800
LC2.1	8	2.55	9.86	0	Irreg. wave	3600
LC2.2	14	3.62	10.29	0	Irreg. wave	3600
LC2.3	18	4.44	10.66	0	Irreg. wave	3600
LC3.1	8	2.55	9.86	0.17	Irreg. wave	3600
LC3.2	14	3.62	10.29	0.13	Irreg. wave	3600
LC3.3	18	4.44	10.66	0.12	Irreg. wave	3600

For steady wind conditions, the normal wind profile (NWP) was applied, in which the wind profile $U(z)$ is the average wind speed as a function of height z above mean sea level (MSL), and is given by the following power law

$$U(z) = U_{ref} \left(\frac{z}{z_{ref}} \right)^{\alpha} \tag{27}$$

where U_{ref} is the reference wind speed, z_{ref} is the height of reference wind speed and α is the power law exponent. In this study z_{ref} is set to be 79.78 m, which is the vertical center of blades above MSL. The value of α was chosen to be 0.14 for the floating wind turbines according to IEC 61400-3 [35]. For turbulent wind conditions, the TurbSim was used to generate the three dimensional turbulent wind field according to the Kaimal turbulence model for IEC Class C. Regarding the irregular wave conditions, the irregular wave history was generated using the JONSWAP wave model. The significant wave height and peak period were set based on their correlation with wind speed for the Statfjord site in the northern North Sea [36].

4.3. Verification using the landbased VAWT

The landbased VAWT is firstly used to study the capability of the code SIMO-RIFLEX-AC to calculate the aerodynamic loads accurately. Three fully coupled aero-hydro-servo-elastic codes are considered here, i.e. SIMO-RIFLEX-DMS, SIMO-RIFLEX-AC and HAWC2. The code SIMO-RIFLEX-DMS calculates the aerodynamic loads using the DMS method with the Beddoes-Leishman dynamic stall model. While the HAWC2 computes the aerodynamic loads using the AC method with the Stig Øye dynamic stall model. An overview of the capability of these three codes are demonstrated in table 4.

Table 4: Description of three codes

	SIMO-RIFLEX-DMS	SIMO-RIFLEX-AC	HAWC2
Aerodynamics (aero)	DMS+BL DS	AC+BL DS	AC+Stig Øye DS
Hydrodynamics (hydro)	Airy + PF + ME	Airy + PF + ME	Airy + ME
Structural dynamics (elastic)	FEM	FEM	MB
Control system (servo)	UD DLL	UD DLL	UD DLL

DMS: Double multi-streamtube; AC: Actuator cylinder; DS: Dynamic stall; BL: Beddoes-Leishman; Airy: Airy wave theory; PF: Potential flow; ME: Morison's equation; FEM: Finite element method; MB: Multi-body system; UD DLL: user defined external dynamic link library

LC1 with steady wind is carried out using each code for the landbased VAWT, respectively. LC1.1, LC1.2 and LC1.3 are three representative operational conditions with a wind speed that is below, equal to and above the rated wind speed, respectively. The corresponding typical tip speed ratios are 4.39, 2.51 and 1.95. The adaptation of the Beddoes-Leishman dynamic stall model has been studied for VAWTs by Dyachuk et al. [20], However, dynamic stall model implemented in HAWC2 is developed for HAWTs and does not seem to work reliably for VAWTs [37], the simulations of the landbased VAWT are thus carried out without considering the effect of dynamic stall. Time histories of the rotor rotational speed, thrust, side force and aerodynamic torque calculated using the three codes are compared, as illustrated in Figure 8 -9.

For the considered two-bladed rotor, the aerodynamic loads vary periodically from approximate zero to double the mean value. These periodic aerodynamic loads cause the periodic variation in the rotor rotational speed. Due to the robust controller implemented, the amplitude of this variation is very small compared to the mean value. It is thus assumed that the small variation in the rotor rotational speed does not affect the aerodynamic loads, including the thrust and aerodynamic torque.

For load cases with low tip speed ratio such as LC1.2 and LC1.3, these three codes agree well with each other in the thrust and aerodynamic torque. This can be observed in Figure 8, which shows the thrust force, side force and aerodynamic torque computed using these three codes when ignoring the effect of dynamic stall. However, at load cases with relatively high tip speed ratio such as LC1.1, these three codes present notable differences in terms of the thrust force, side force and aerodynamic torque, as shown in Figure 9. When neglecting the effect of dynamic stall, HAWC2 predicts a smaller thrust and aerodynamic torque than the codes SIMO-RIFLEX-AC and SIMO-RIFLEX-DMS. Moreover, the thrusts computed using SIMO-RIFLEX-AC and SIMO-RIFLEX-DMS are very close to each other. In addition, the peak values of the aerodynamic torque predicted using SIMO-RIFLEX-AC and SIMO-RIFLEX-DMS are very close and much larger than that by HAWC2. And HAWC2 predicts a valley value of aerodynamic torque that is much larger than zero.

In order to reveal the essential reasons that result in the different resultant aerodynamic loads, the normal load and tangential load acting on the blade element are studied, as shown in Figure 10 and 11. Figure 10 shows the time history of blade normal and tangential loads at the midpont of the blade simulated using the codes SIMO-RIFLEX-AC and HAWC2. it is obvious that the negative normal loads differ notably. The possible reason for this deviation is that the code SIMO-RIFLEX-AC accounts for the tangential term when calculating the induced velocity, while HAWC2 ignores it. It has been shown by Cheng et al. [16] that including the tangential term when calculating the induced velocity can modify the behavior of normal loads in the downwind part

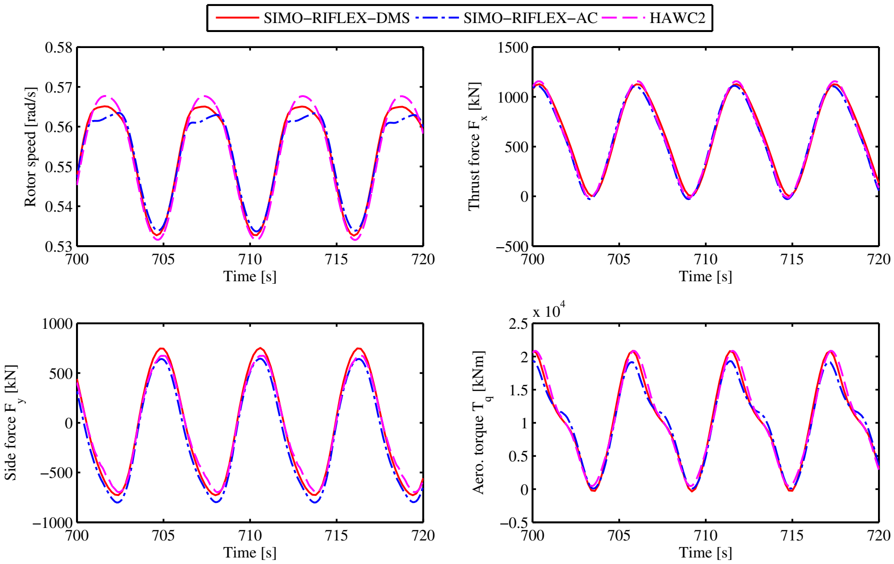

Figure 8: Comparison of the rotational speed, thrust, side force and aerodynamic torque of the landbased VAWT using three codes without considering the effect of dynamic stall in LC1.2 .

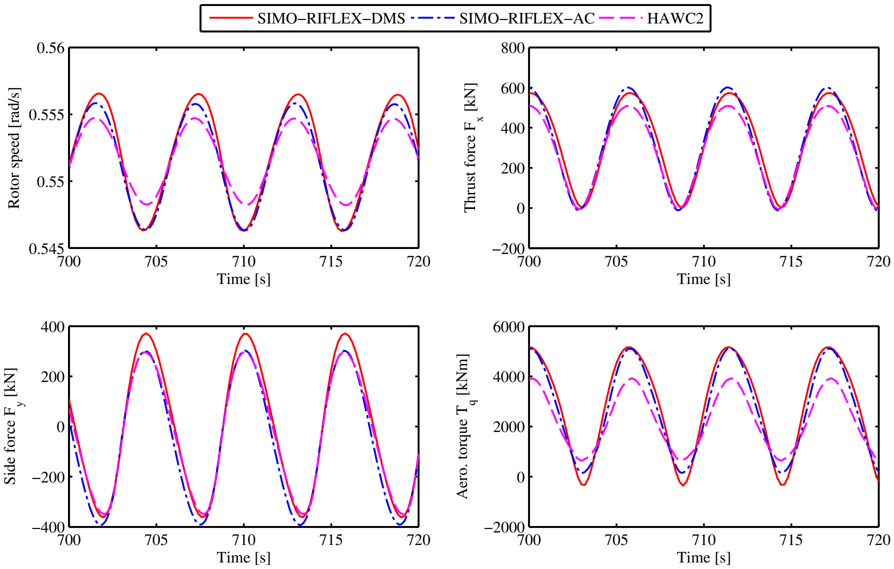

Figure 9: Comparison of the rotational speed, thrust, side force and aerodynamic torque of the landbased VAWT using three codes without considering the effect of dynamic stall in LC1.1.

as depicted in Figure 10, which corresponds to negative normal loads.

In Figure 11, the distribution of the normal and tangential loads along the blade are demonstrated when the rotor encounters the largest and smallest aerodynamic torque, which are denoted as peak and valley, respectively. It can be observed that the distribution of the normal and tangential loads along the blade are not smooth, showing a large number of small peaks. This is due to the blade elasticity considered in the present study. The blade deforms when the blade suffers from the aerodynamic loads, consequently the inclination of the elements within the blade is not very continuous and has some peaks, which ultimately results in the small peaks in the distribution of loads along the blades. The codes SIMO-RIFLEX-AC and HAWC2 differs in the normal and, especially, tangential loads. It's the tangential force that mainly contributes to the aerodynamic torque, consequently the aerodynamic torque differs a lot. The distributions of normal and tangential loads are not symmetric because of the wind shear and blade elasticity. Moreover, the part with the position r/S approximately ranging from 0.35 to 0.85 is the main contribution for the tangential load.

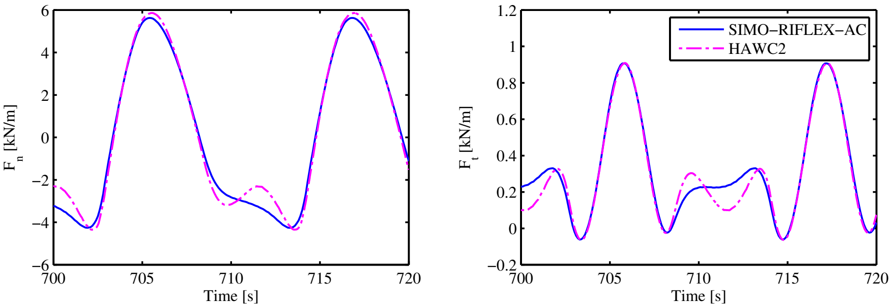

Figure 10: Comparison of simulated blade forces in normal and tangential direction at mid-point of the blade using SIMO-RIFFLEX-AC and HAWC2 in LC1.1, the effect of dynamic stall is not considered.

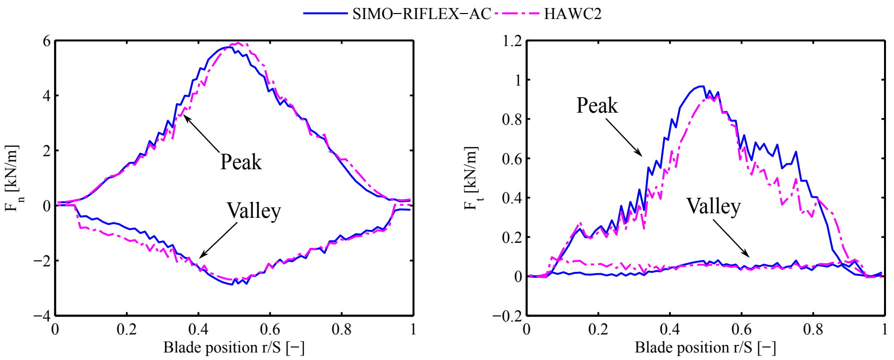

Figure 11: Distribution of the normal and tangential forces along the blade at the peak and valley value of aerodynamic torque using SIMO-RIFFLEX-AC and HAWC2 in LC1.1, the effect of dynamic stall is not considered.

4.4. Verification using the semi VAWT

In this section, the semi VAWT is used to verifiy the capability of the code SIMO-RIFLEX-AC. Only the code SIMO-RIFLEX-DMS is considered, since it models the hydrodynamics, structural mechanics and controller dynamics in the same way as the code SIMO-RIFLEX-AC. This verification starts from the steady wind only LCs.

4.4.1. Steady wind cases

LC1 with steady wind is firstly carried out for the semi VAWT using the codes SIMO-RIFLEX-AC and SIMO-RIFLEX-DMS. It aims to investigate the capability of SIMO-RIFLEX-AC to predict the wind-induced responses, including the platform motions, structural responses and wind turbine performance.

Figure 12 shows the mean values and standard deviations of the generator power, thrust, side force and aerodynamic torque acting on the semi VAWT in LC1. The mean values of the thrust predicted using SIMO-RIFLEX-AC are a little smaller than those by SIMO-RIFLEX-DMS. But SIMO-RIFLEX-AC gives a little larger standard deviation of thrust in LC1.1, which corresponds to load cases with high tip speed ratios. SIMO-RIFLEX-AC also predicts a little larger mean aerodynamic torque in LC1.3. Visible difference lies in the mean value of side force, especially in LC1.1 where SIMO-RIFLEX-AC gives a negative side force while SIMO-RIFLEX-DMS predicts almost zero side force. These differences result from three possible reasons: one is that AC method predicts smaller aerodynamic loads than the DMS method; another one is that the DMS method essentially neglects the lateral induction, which has some influence on the side force. The last one is that the code SIMO-RIFLEX-DMS assumes that the rotor always holds upright even though the tower is inclined due to the roll or pitch motions of the platform, since Wang et al. [2] stated that the effect of tower tilt on the aerodynamic coefficients of the rotor studied is considered negligible up to a tilt angle of 10°. In addition, the code SIMO-RIFLEX-DMS does not account for the effect of dynamic inflow.

In LC1, the platform motions are wind-induced and present similar trends as the aerodynamic loads, as illustrated in Figure 13. The code SIMO-RIFLEX-AC predicts smaller mean values in surge, heave, pitch and yaw motions than the code SIMO-RIFLEX-DMS. However, the sway and roll motions show notable differences since these two codes predict significant different mean values in the side force. Similar trends are also find in the structural responses, such as the tower base fore-aft bending moment M_{FA} and side-side bending moment M_{SS}. The code SIMO-RIFLEX-AC gives a little smaller values in the mean value and standard deviation of M_{FA}, and the standard deviation of M_{SS}. In addition, the mean value of M_{SS} is significantly different.

4.4.2. Combined wind and wave cases

The combined wind and wave cases, i.e. the LC2 and LC3, are then used to verify the capability of the code SIMO-RIFLEX-AC to capture the stochastic variations of the dynamic responses. Identical wind and wave time series are used for the codes SIMO-RIFLEX-DMS and SIMO-RIFLEX-AC. For each load case, five different seeds are employed to reduce the stochastic variation in the results.

Figure 14 compares the mean values of the generator power for the semi VAWT in LC1, LC2 and LC3 with the error bar indicating the standard de-

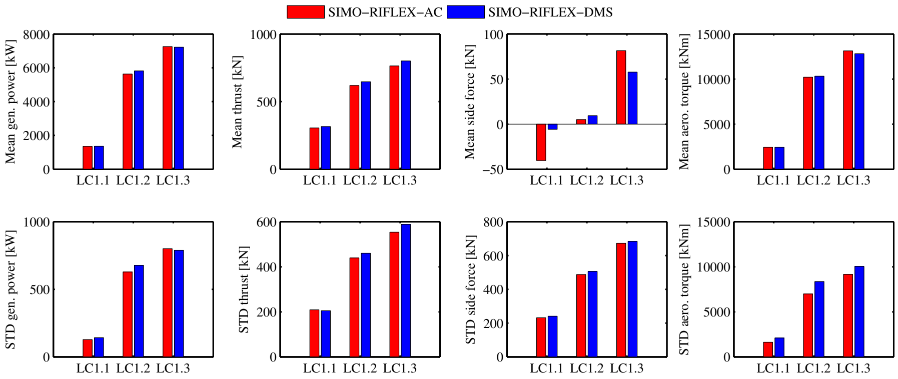

Figure 12: Mean values and standard deviations of the generator power, aerodynamic thrust, side force and torque acting on the semi VAWT in LC1.

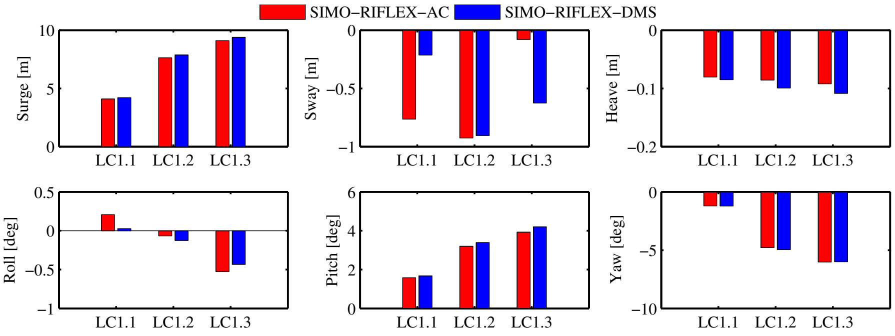

Figure 13: Mean values of platform motions of the semi VAWT in LC1 .

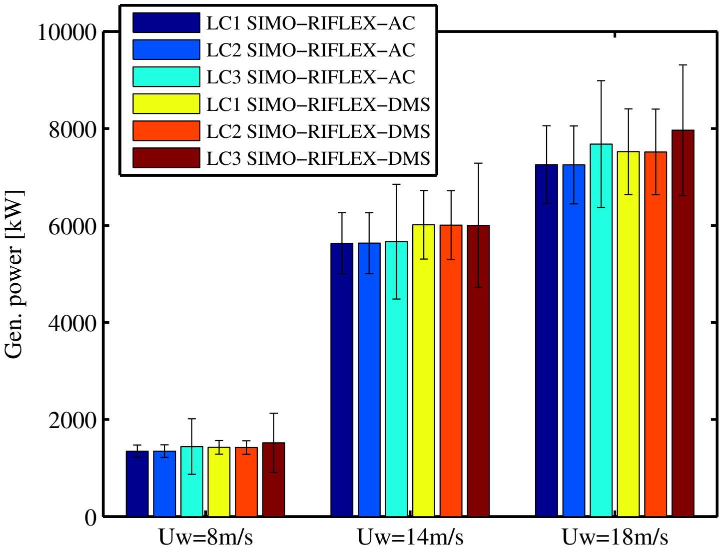

Figure 14: Mean value and standard deviation of the generator power for the semi VAWT in LC1, LC2 and LC3. The error bar indicates the standard deviation from the mean value.

viation. It can be found that at a certain mean wind speed, LC1 and LC2 gives very close mean value and standard deviation in the generator power for both codes, which implies that wave loads have slight influence on the generator power. Moreover, in LC3 the mean value and standard deviation of the generator power all increase to some extent than the steady wind cases LC1 and LC2. In addition, the code SIMO-RIFLEX-AC predicts smaller mean values of the generator power than the code SIMO-RIFLEX-DMS while the standard deviation estimated by these two codes are very close.

In Figure 15, the mean value and standard deviation of the aerodynamic thrust, side force and torque are shown for the semi VAWT in LC3 with turbulent wind and irregular waves. The trends observed in Figure 15 are quite similar as those in Figure 12. Compared to the steady wind only cases, the mean value of the side force in the turbulent wind and irregular wave cases are different, this is mainly due to changes in aerodynamic loads resulting from the wind turbulence, because the irregular waves cause negligible lateral wave loads.

Rigid body motions of the semi VAWT are also of concern. The mean values

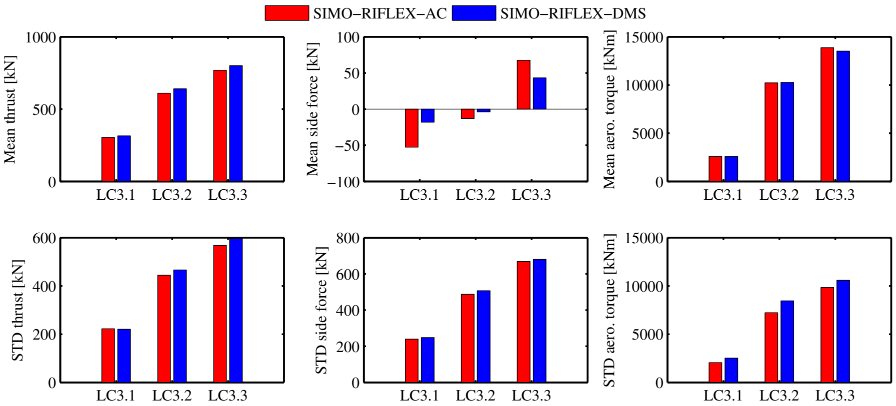

Figure 15: Mean value and standard deviation of the aerodynamic thrust, side force and torque for the semi VAWT in LC3

and standard deviations of the platform motions are shown in Figure 16. The mean values of the platform motions are quite close to the mean values in the steady wind only conditions, since the mean value of these platform motions are highly dependent on wind loads.

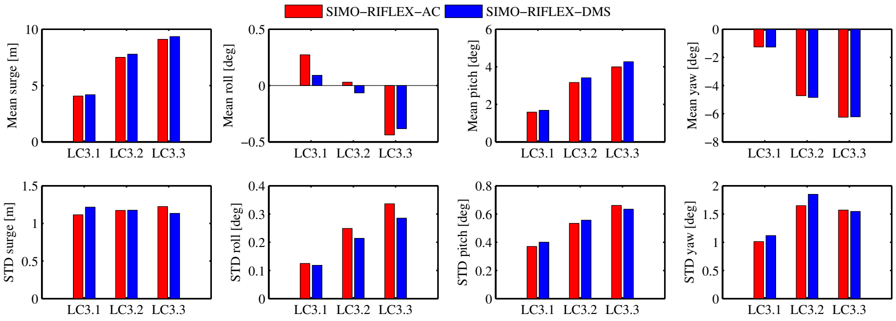

Figure 16: Mean value and standard deviation of the surge, roll, pitch and yaw motions of the semi VAWT in LC3

Though the standard deviation of the thrust given by the code SIMO-RIFLEX-AC is smaller than those given by the code SIMO-RIFLEX-DMS, the code SIMO-RIFLEX-AC gives a smaller standard deviation of surge and pitch motions in LC3.1 and LC3.2, but predicts a little larger in LC3.3. This is due to the fact that the code SIMO-RIFLEX-DMS omits the effect of tower tilt when

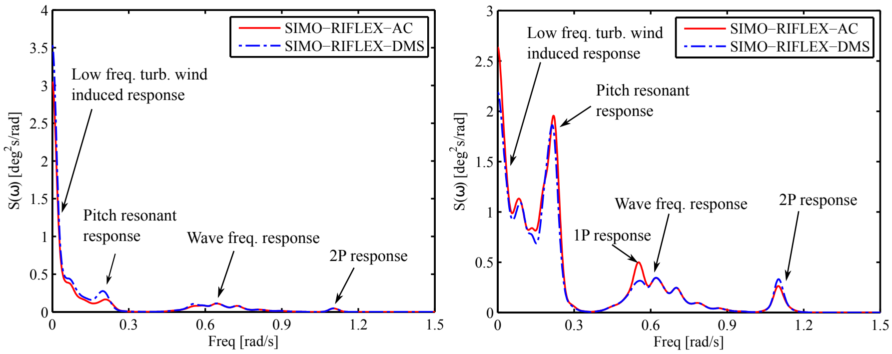

(a) LC3.1: $U_W = 8$ m/s, $H_S = 2.55$ m, $T_P = 9.86$ s

(b) LC3.3: $U_W = 18$ m/s, $H_S = 4.44$ m, $T_P = 10.66$ s

Figure 17: Power spectra of the pitch motion of the semi VAWT in (a) LC3.1 and (b) LC3.3

calculating the aerodynamic loads. However, as the wind speed increases, the effect of tower tilt on aerodynamic loads as well as platform motions becomes more important. This can also be observed using the power spectrum analysis, as the power spectra of pitch motions demonstrated in Figure 17. The wave frequency response predicted by these two codes agrees very well. Visible differences are found in the low frequency region, which is mainly induced by the low frequency turbulent wind. When the wind speed is relatively small, the effect of tower tilt on platform motion is very small, the low frequency response given by the code SIMO-RIFLEX-DMS is larger due to the larger aerodynamic loads predicted by the DMS method, as shown in Figure 17(a). However, as the wind speed becomes larger, which causes the larger platform pitch motion, the effect of tower tilt becomes more significant and gives larger low frequency response.

Moreover, the code SIMO-RIFLEX-AC predicts larger standard deviation of roll motion in LC3 than the code SIMO-RIFLEX-DMS. Power spectral analysis of roll in LC3.2, as illustrated in Figure 18, reveals that the code SIMO-RIFLEX-DMS contributes a little bigger 2P response, whereas the low frequency turbulent wind induced response is much smaller than that given by the code SIMO-RIFLEX-AC. A small 1P response is captured by both codes as well. With respect to the yaw motion, the responses are dominated by the yaw resonant response and low frequency turbulent wind induced response. In LC3.1

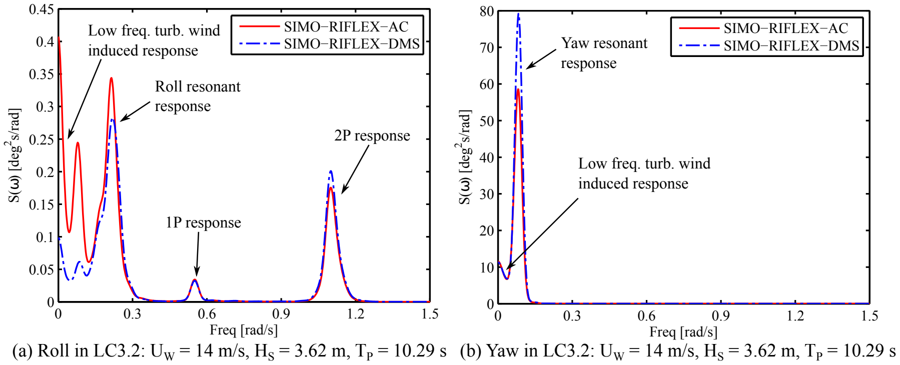

(a) Roll in LC3.2: U_W = 14 m/s, H_S = 3.62 m, T_P = 10.29 s (b) Yaw in LC3.2: U_W = 14 m/s, H_S = 3.62 m, T_P = 10.29 s

Figure 18: Power spectra of the roll and yaw motions of the semi VAWT in LC3.2. (a) roll motion, (b) yaw motion.

and LC3.2, the yaw resonant responses given by the code SIMO-RIFLEX-DMS are much larger than those by the code SIMO-RIFLEX-AC, the corresponding standard deviations of yaw motion are thus also bigger. However, in LC3.3 the code SIMO-RIFLEX-AC gives a little larger standard deviation of yaw motion, power spectral analysis shows that in LC3.3 the yaw resonant response predicted by the two codes are comparable while the code SIMO-RIFLEX-AC gives a little larger low frequency turbulent wind induced yaw motion.

For floating wind turbines, the tower base bending moment is caused by the large aerodynamic force acting on the rotor and by the weight of the rotor due to the tower tilt. The codes SIMO-RIFLEX-AC and SIMO-RIFLEX-DMS predict different aerodynamic loads and tower tilt angle, consequently the tower base bending moments are different. Figure 19 gives the mean value and standard deviation of the tower base fore-aft bending moment M_{FA} and side-side bending moment M_{SS}. The code SIMO-RIFLEX-AC gives a little smaller values than the code SIMO-RIFLEX-DMS in the mean value and standard deviation of M_{FA}. The percentage difference of the mean value of the M_{FA} between the codes SIMO-RIFLEX-AC and SIMO-RIFLEX-DMS is 6.5%, 8.0% and 6.9% for the LC3.1, LC3.2 and LC3.3, respectively. Regarding the M_{SS}, the mean value of M_{SS} is significantly different. Moreover, the percentage difference of the standard deviation of the M_{SS} between the codes SIMO-RIFLEX-AC and SIMO-RIFLEX-DMS is 6.7%, 7.8% and 6.4%, respectively. This also implies that the code SIMO-RIFLEX-DMS can over estimate the fatigue damage.

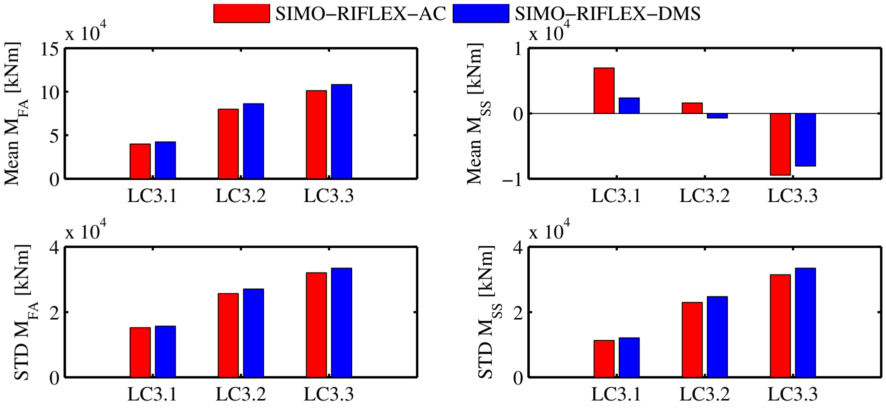

Figure 19: Mean values and standard deviations of tower base fore-aft bending moment M_{FA} and side-side bending moment M_{SS} of the semi VAWT in LC3

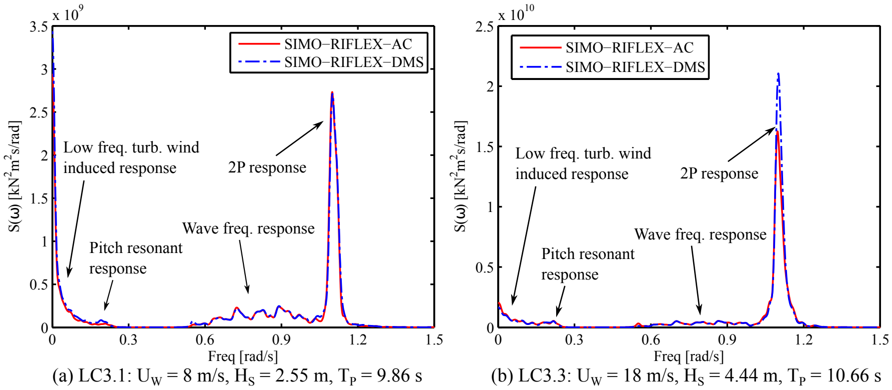

(a) LC3.1: U_W = 8 m/s, H_S = 2.55 m, T_P = 9.86 s (b) LC3.3: U_W = 18 m/s, H_S = 4.44 m, T_P = 10.66 s

Figure 20: Power spectra of tower base fore-aft bending moment for the semi VAWT in (a) LC3.1 and (b) LC3.3

525 Power spectrum analyses of the M_{FA} and M_{SS} are also performed, as depicted in Figure 20. It can be observed that the wave frequency response computed using these two codes matches very well with each other. Visible differences result from the low frequency turbulent wind induced response and,

especially, the 2P response. The responses of M_{FA} are mainly dominated by the wind loads and the contribution of 2P response increases dramatically as the mean wind speed increases. In LC3.1, the code SIMO-RIFLEX-AC gives a slightly larger peak in the 2P response, but also a much smaller low frequency turbulent wind induced response, as shown in Figure 20(a). As a result, the standard deviation of the M_{FA} predicted by the code SIMO-RIFLEX-AC is smaller than that by the code SIMO-RIFLEX-DMS. However, when it comes to LC3.3, the 2P response predicted by the code SIMO-RIFLEX-DMS is otherwise much larger. With respect to the responses of the M_{SS}, the 2P response is extremely dominating and the code SIMO-RIFLEX-DMS alway overestimates the standard deviation of the M_{SS}.

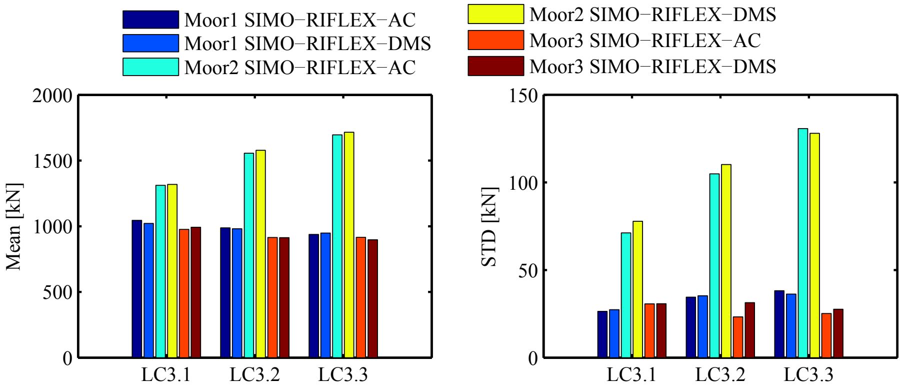

Figure 21: Mean values and standard deviations of tension in mooring lines for the semi VAWT in LC3

Three catenary mooring lines are used to keep the platform in position, as depicted in Figure 7. Among them the mooring line 2 is deployed with direction aligned with the incoming wind. Therefore the mooring line 2 carries the largest tension with respect to both the mean value and the standard deviation, as shown in Figure 21. Due to the yaw motion, the tension in the mooring line 1 is also larger than that in the mooring line 3. Considering the mooring line 2, the code SIMO-RIFLEX-AC predicts a smaller mean value of tension in LC3. Moreover, it also gives smaller standard deviations in LC3.1 and LC3.2, however

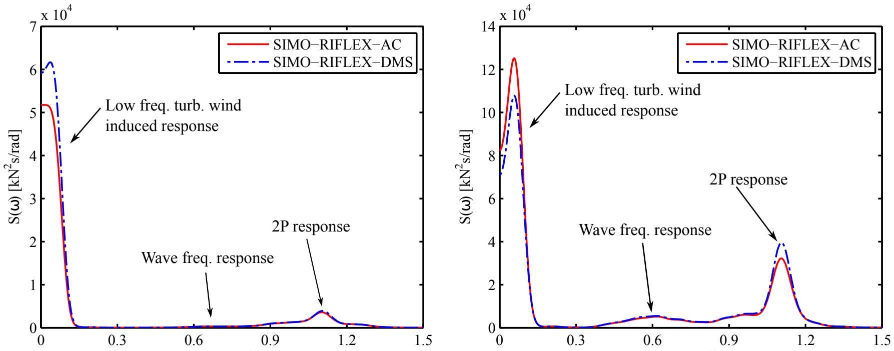

(a) LC3.1: U_W = 8 m/s, H_S = 2.55 m, T_P= 9.86 s (b) LC3.3: U_W = 18 m/s, H_S = 4.44 m, T_P= 10.66 s

Figure 22: Power spectra of tension in mooring line 2 for the semi VAWT in (a) LC3.1 and (b) LC3.3

in LC3.3 the code SIMO-RIFLEX-AC predicts a little larger standard deviation of tension in mooring line 2. Power spectral analysis of the tension shows that the wave frequency response matches very well for these two code, but the total response is dominated by the low frequency turbulent wind induced response and the 2P response, which are both related to the aerodynamic loads. In LC3.1 and LC3.2, the code SIMO-RIFLEX-AC gives smaller low frequency response, whereas it predicts relatively larger low frequency response in LC3.3.

5. Conclusions

This paper deals with the development and verification of a fully coupled method for modeling and dynamic analysis of floating vertical axis wind turbines (VAWTs). Based on the actuator cylinder (AC) flow model, an aerodynamic code AC is developed and then coupled with the code SIMO-RIFLEX to achieve a fully integrated simulation tool to evaluate the performance of floating VAWT systems. The code SIMO-RIFLEX-AC can account for the turbulent wind inflow, aerodynamics, hydrodynamics, structural dynamics and control dynamics.

Details regarding the induction calculation in the AC model is firstly described in this paper. When calculating the linear induced velocities, contributions from not only the normal load but also the tangential load are taken into account. A new modified linear solution is proposed to better correct the linear solution. Using the AC method, aerodynamic modeling of floating VAWTs is established with consideration of the effects of wind shear, turbulence and dynamic inflow. The Beddoes-Leishman dynamic stall model is also implemented to account for the unsteady aerodynamic effect.

The developed aerodynamic code is then coupled with SIMO-RIFLEX to achieve a fully coupled aero-hydro-servo-elastic simulation tool, i.e. SIMO-RIFLEX-AC. It calculates the 1st and 2nd order hydrodynamic loads using potential flow theory and viscous force using the Morison's equation. The blades, tower, shaft and mooring lines are modeled using flexible finite element and solved using the Newmark-β method. Also implemented is a controller that can enable variable-speed fixed-pitch operation.

Finally the developed code SIMO-RIFLEX-AC is verified by a series of code-to-code comparisons. Both a landbased VAWT and a semi VAWT are considered. Using the landbased VAWT, the code SIMO-RIFLEX-AC is verified by comparison with the codes SIMO-RIFLEX-DMS and HAWC2. It shows that the code SIMO-RIFLEX-DMS predicts larger lateral force and aerodynamic torque, especially at load cases with relatively high tip speed ratio. At load cases with low tip speed ratio, these three codes agree well with each other. Considering the semi VAWT, the code SIMO-RIFLEX-AC is verified with the code SIMO-RIFLEX-DMS. Comparative study reveals that these two code give relatively close dynamic responses. Moreover, because of neglecting the effect of tower tilt and the essential characteristics of the DMS method, the code SIMO-RIFLEX-DMS predicts larger surge, heave and pitch motions, tower base fore-aft bending moment and tension in mooring line 2. At load cases with high tip speed ratio, it also overpredicts the aerodynamic torque, the generator power, as well as the yaw motion. In addition, the code SIMO-RIFLEX-DMS also predicts larger the fatigue damage at the tower base.

Acknowledgment

The authors would like to acknowledge the financial support from the EU FP7 project MARE WINT (project NO. 309395) through the Centre for Ships and Ocean Structures (CeSOS) and Centre for Autonomous Marine Operations and Systems (AMOS) at the Department of Marine Technology, Norwegian University of Science and Technology (NTNU), Trondheim, Norway. The first author would like to thank the Department of Wind Energy for kindly hosting me and valuable discussions with senior scientist Torben J. Larsen at the Technical University of Denmark, Roskilde, Denmark. The first author would also appreciate the kindly help on the coupling between the codes RIFLEX and AC from Associate Prof. Erin Bachynski at NTNU and Dr. Kai Wang at Aker Solutions.

References

[1] J. Paquette, M. Barone, Innovative offshore vertical-axis wind turbine rotor project, EWEA 2012 Annual Event.

[2] K. Wang, M. O. L. Hansen, T. Moan, Model improvements for evaluating the effect of tower tilting on the aerodynamics of a vertical axis wind turbine, Wind Energy 18 (2015) 91–110. `doi:10.1002/we.1685`.

[3] J. O. Dabiri, Potential order-of-magnitude enhancement of wind farm power density via counter-rotating vertical-axis wind turbine arrays, Journal of Renewable and Sustainable Energy 3 (4) (2011) 043104. `doi:10.1063/1.3608170`.

[4] M. Borg, A. Shires, M. Collu, Offshore floating vertical axis wind turbines, dynamics modelling state of the art. part i: Aerodynamics, Renewable and Sustainable Energy Reviews`doi:10.1016/j.rser.2014.07.096`.

[5] K. Wang, T. Moan, M. O. L. Hansen, A method for modeling of floating vertical axis wind turbine, in: Proceedings of the 32th International Conference on Ocean, Offshore and Arctic Engineering, 2013.

[6] M. Collu, M. Borg, A. Shires, F. P. Brennan, Flovawt: progress on the development of a coupled model of dynamics for floating offshore vertical axis wind turbines, in: Proceedings of the ASME 2013 32nd International Conference on Ocean, Offshore and Arctic Engineering, 2013.

[7] B. C. Owens, J. E. Hurtado, J. A. Paquette, D. T. Griffith, M. Barone, Aeroelastic modeling of large offshore vertical-axis wind turbines: development of the offshore wind energy simulation toolkit, in: Proceedings of the 54th AIAA Structures, Structural Dynamics and Materials Conference, 2013.

[8] MARINTEK, Simo-theory manual version 4.0 (2012).

[9] MARINTEK, Rifelx theory manual, version 4.0 (2012).

[10] C. S. Ferreira, H. A. Madsen, M. Barone, B. Roscher, P. Deglaire, I. Arduin, Comparison of aerodynamic models for vertical axis wind turbines, Journal of Physics: Conference Series 524 (1) (2014) 012125.

[11] B. Roscher, Current aerodynamic models for VAWT and numerical comparison between HAWC2 and U2DiVA, Special project - EWEM rotor design (2014).

[12] H. A. Madsen, The Actuator Cylinder: A flow model for vertical axis wind turbines, Institute of Industrial Constructions and Energy Technology, Aalborg University Centre, 1982.

[13] H. A. Madsen, T. J. Larsen, U. S. Paulsen, L. Vita, Implementation of the actuator cylinder flow model in the HAWC2 code for aeroelastic simulations on vertical axis wind turbines, in: 51st AIAA Aerospace Sciences Meeting including the New Horizons Forum and Aerospace Exposition, 2013. `doi:10.2514/6.2013-913`.

[14] T. J. Larsen, H. A. Madsen, On the way to reliable aeroelastic load simulation on VAWT's, in: Proceedings of EWEA, 2013.

[15] U. S. Paulsen, H. A. Madsen, J. H. Hattel, I. Baran, P. H. Nielsen, Design optimization of a 5 mw floating offshore vertical-axis wind turbine, Energy Procedia 35 (2013) 22–32. `doi:10.1016/j.egypro.2013.07.155`.

[16] Z. Cheng, H. A. Madsen, Z. Gao, T. Moan, Aerodynamic modeling of offshore vertical axis wind turbines using the actuator cylinder method, Energy Procedia 94 (2016) 531–543.

[17] B. J. Jonkman, Turbsim user's guide: Version 1.50. (2009).

[18] J. G. Leishman, T. S. Beddoes, A semi-empirical model for dynamic stall, Journal of the American Helicopter Society 34 (3) (1989) 3–17. `doi:10.4050/JAHS.34.3`.

[19] S. Gupta, J. G. Leishman, Dynamic stall modelling of the s809 aerofoil and comparison with experiments, Wind Energy 9 (6) (2006) 521–547. `doi:10.1002/we.200`.

[20] E. Dyachuk, A. Goude, H. Bernhoff, Dynamic stall modeling for the conditions of vertical axis wind turbines, AIAA Journal 52 (1) (2014) 72–81. `doi:10.2514/1.j052633`.

[21] P. J. Moriarty, A. C. Hansen, AeroDyn theory manual, NREL/TP-500-36881 (2005).

[22] N. Luxcey, H. Ormberg, E. Passano, Global analysis of a floating wind turbine using an aero-hydro-elastic numerical model: Part 2 benchmark study, in: Proceedings of the 30th International Conference on Ocean, Offshore and Arctic Engineering, 2011.

[23] H. Ormberg, E. Passano, N. Luxcey., Global analysis of a floating wind turbine using an aero-hydro-elastic model: Part 1 code development and case study, in: Proceedings of the 30th International Conference on Ocean, Offshore and Arctic Engineering, 2011.

[24] E. E. Bachynski, Design and dynamic analysis of tension leg platform wind turbines, PhD thesis, Norwegian University of Science and Technology (2014).

[25] W. E. Cummins, The impulse response function and ship motions, Institut fur schiffbau, universitat hamburg, hamburg (1962).

[26] O. M. Faltinsen, Sea loads on ships and offshore structures, Cambridge University Press, Cambridge, UK, 1995.

[27] A. Robertson, J. Jonkman, M. Masciola, H. Song, A. Goupee, A. Coulling, C. Luan, Definition of the semi-submersible floating system for phase II of OC4, Report (2012).

[28] Z. Cheng, K. Wang, Z. Gao, T. Moan, A comparative study on dynamic responses of spar-type floating horizontal and vertical axis wind turbines, Wind Energy 20 (2) (2017) 305–323.

[29] L. Vita, Offshore floating vertical axis wind turbines with rotating platform, Phd thesis, Technical University of Denmark (2011).

[30] Z. Cheng, K. Wang, Z. Gao, T. Moan, Dynamic response analysis of three floating wind turbine concepts with a two-bladed darrieus rotor, Journal of Ocean and Wind Energy 2 (2015) 213–222. `doi:10.17736/jowe.2015.jcr33`.

[31] K. Wang, Modeling and dynamic analysis of a semi-submersible floating vertical axis wind turbine, PhD thesis, Norwegian University of Science and Technology (2015).

[32] K. Wang, Z. Cheng, T. Moan, M. O. L. Hansen, Effect of difference-frequency forces on the dynamics of a semi-submersible type FVAWT in misaligned wave-wind condition, in: Proceedings of the 25th International Ocean and Polar Engineering Conference, 2015.

[33] J. M. Jonkman, S. Butterfield, W. Musial, G. Scott, Definition of a 5-mw reference wind turbine for offshore system development, Tech. Rep. NREL/TP-500-38060, NREL, Golden, CO, USA (2009).

[34] Abaqus users manual. version 6.10. abaqus inc (2010).

[35] IEC, International standard 61400-1, wind turbines, part 1: Design requirements (2005).

[36] K. Johannessen, T. S. Meling, S. Haver, Joint distribution for wind and waves in the northern north sea, International Journal of Offshore and Polar Engineering 12 (1).

[37] D. Verelst, H. A. Madsen, M. Borg, U. S. Paulsen, H. G. Svendsen, P. A. Berthelsen, integrated simulation challenges with the deepwind floating vertical axis wind turbine, Energy Procedia 80 (2015) 321–328.